Int J CARS (2015) 10:1515–1526
DOI 10.1007/s11548-015-1151-z

ORIGINAL ARTICLE

Computer-aided analysis of prostate multiparametric MR images: an unsupervised fusion-based approach

N. Betrouni · N. Makni · S. Lakroum · S. Mordon · A. Villers · P. Puech

Received: 25 August 2014 / Accepted: 6 January 2015 / Published online: 22 January 2015

Abstract
Objective The aim of this study is to provide an automatic framework for computer-aided analysis of multiparametric magnetic resonance (mp-MR) images of prostate.
Method We introduce a novel method for the unsupervised analysis of the images. An evidential C-means classifier was adapted for use with a segmentation scheme to address multisource data and to manage conflicts and redundancy.
Results Experiments were conducted using data from 15 patients. The evaluation protocol consisted in evaluating the method abilities to classify prostate tissues, showing the same behaviour on the mp-MR images, into homogeneous classes. As the actual diagnosis was available, thanks to the correlation with histopathological findings, the assessment focused on the ability to segment cancer foci. The method exhibited global sensitivity and specificity of 70 and 88 %, respectively.
Conclusion The preliminary results obtained by these initial experiments showed that the method can be applied in clinical routine practice to help making decision especially for practitioners with limited experience in prostate MRI analysis.

N. Betrouni (✉) · N. Makni · S. Lakroum · S. Mordon · A. Villers · P. Puech
INSERM, U703, 152, rue du Docteur Yersin, 59120, Loos, CHRU de Lille, France
e-mail: nacim.betrouni@inserm.fr; n-betrouni@chru-lille.fr

N. Betrouni · S. Mordon · A. Villers · P. Puech
Université de Lille II, Lille, France

P. Puech
Radiology Department, Hôpital Claude Huriez, Lille University Hospital, Lille, France

A. Villers
Urology Department, Hôpital Claude Huriez, Lille University Hospital, Lille, France

Keywords Computer-aided analysis · Prostate cancer · Multiparametric MR images · Evidential C-means classifier

Introduction

A current challenge in prostate cancer is the development of new strategies to improve the diagnosis of significant cancers while excluding insignificant ones. Presently, a volume threshold is used, and cancers more than 0.5 cc are considered as significant. Systematic transrectal ultrasound biopsies (TRUS-B) remain the gold standard for prostate cancer diagnosis; however, these biopsies are invasive and miss a significant percentage of cancers. In contrast, prostate magnetic resonance imaging (MRI) can be used noninvasively for reliable characterization of prostate tissues/lesions, by taking advantage of multiparametric protocols [1].

A typical prostate multiparametric MR study includes a morphological T2-weighted (T2-W) series and a functional series, including diffusion-weighted imaging (DWI) sequences and perfusion T1-weighted sequences, acquired before, during and after contrast agent administration (also called dynamic contrast enhanced [DCE] MRI). In some cases, these studies also include spectroscopic analysis. For multiparametric analysis, several DWI sequences with different diffusion gradients are acquired and used to compute the apparent diffusion coefficient (ADC) map. The DCE images are used to analyse the tissue enhancement, either visually or using time/intensity curves and semi-quantitative parameters, such as the area under the enhancement curve, wash in and wash out rates and time to peak. Computation of pharmacokinetic parameters can also be used to characterize tissue microcirculation, for example, using Tofts' model, where K_{trans} is the transfer constant between the blood plasma and the extra-vascular extra-cellular spaces (EES), K_{ep} is

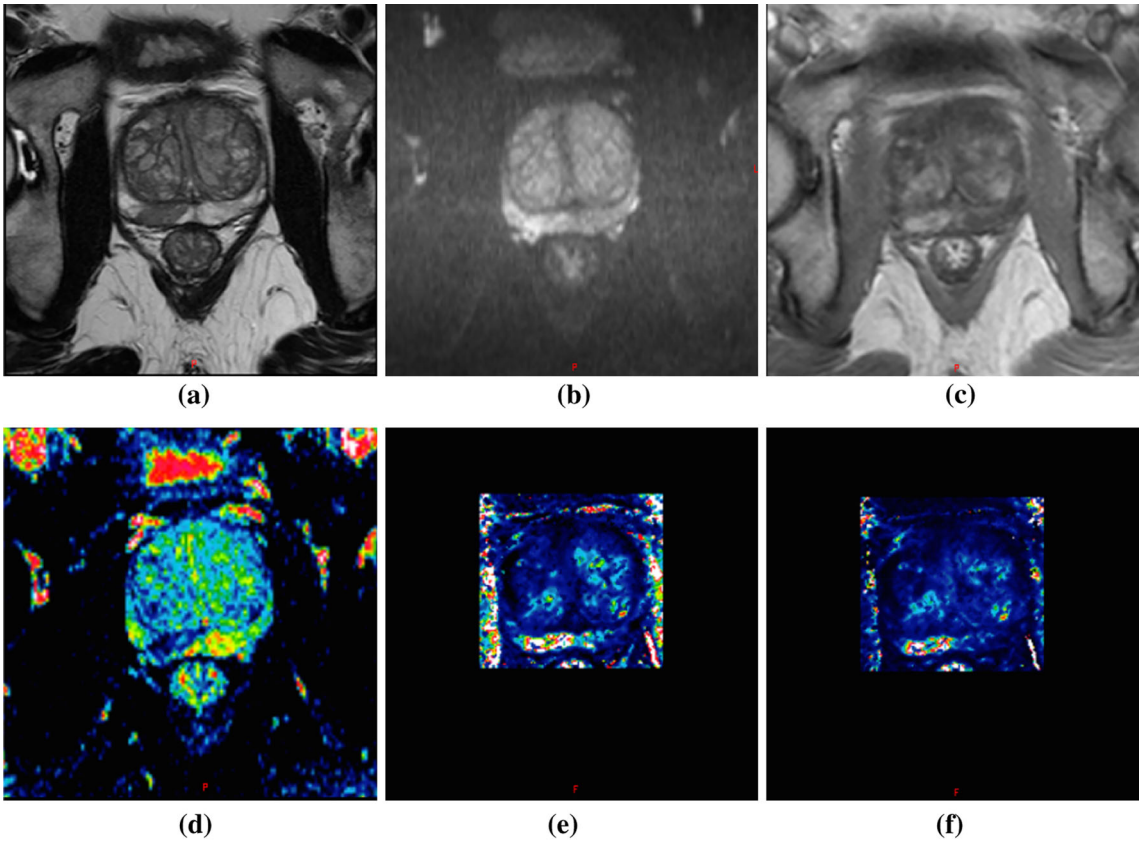

Fig. 1 Examples of multiparametric magnetic resonance images: **a** T2-weighted sequence, **b** diffusion-weighted images (DWI), **c** T1-weighted dynamic contrast enhance (DCE) images, **d** the apparent diffusion coefficient map computed from the diffusion-weighted sequences and **e**, **f** pharmacokinetics parameters computed from the DCE sequences. The transfer constant between the blood plasma and the extra-vascular extra-cellular spaces (K_{trans}) and the exchange constant rate between the extra-vascular extra-cellular spaces and the blood plasma (K_{ep}) were determined in **e** and **f**, respectively

the exchange constant rate between the EES and the blood plasma, and V_e is the extra-vascular extra-cellular volume [2,3] (Fig. 1).

In this context, and because MRI involves an enormous number of data to interpret, many authors have investigated automatic classification algorithms to design MRI-based computer-aided diagnosis (CAD) tools and software for cancer characterization. The current standard paradigm for CAD systems is as a second reader. After the radiologist has evaluated multiple imaging sets, CAD is used to indicate the likelihood that a given suspicious region is malignant. Most of the employed methods are based on supervised classification techniques, in which a set of preinterpreted patient data must be used as a learning step (Table 1). These approaches have presented two main limitations. First, the performance of the algorithm depends on the quality and volume of the training data. Second, the learning step requires retrospective data, which might be either obsolete or centre specific.

In this study, we began with the assumption that a multiparametric approach would be optimal for all of the images. We then proposed an unsupervised method for prostate tissue classification from multiparametric MR images. This method was not designed for the detection of cancer or suspicious lesions but rather was intended to be used as an analysis tool, allowing us to merge information from all available sources to address conflict and redundancy and to provide a unique homogeneous pattern (tissues) map.

We investigated the use of evidence theory. This approach, also known as belief functions theory, is becoming widely used in multisource data analysis. It provides an advanced modelling of fusion, conflicts among sources and outliers [4]. Several applications of this reasoning in medical image analysis and CAD can be found (e.g. in brain MRI segmentation and tumour detection) [5,6]. Our proposed approach is an adaptation of the evidential C-means classifier (ECM) introduced by Masson and Denoeux [7]. We successfully applied this method to multiparametric prostate MR data in a previous work, in which the aim was to segment and separate the prostate into two compartments: peripheral and transition zones [8].

Table 1 State of the art of classification and clustering methods applied for prostate magnetic resonance image analysis

	MR Data	Clustering/classification Algorithms	Region of interest	Validation—correlation with histopathology maps
Supervised				
Chan et al. [9]	T2W, ADC and proton density	Support vectors machine and Fisher linear discriminant	Peripheral zone	No
Madabhushi et al. [10]	Ex vivo MRI	Bayesian + Fusion	Prostate	Yes
Vos et al. [11]	DCE MRI	Support vectors machine	Peripheral zone	Yes
Puech et al. [12]	DCE MRI	Decision tree	Prostate	Yes
Vos et al. [13]	DCE MRI and T2W	Support vectors machine	Peripheral zone	Yes
Lopes et al. [14]	T2W	Support vectors machine and Adaboost	Peripheral zone	Yes
Niaf et al. [15]	T2W, ADC and DCE MRI	4 Classifiers	Peripheral zone	Yes
Shah et al. [16]	T2W, ADC and DCE MRI	Support vectors machine	Peripheral zone	Yes
Chesnais et al. [17]	T2W, ADC and DCE MRI	4 Classifiers (method from Niaf et al. [15])	Peripheral zone	Yes
Hoeks et al. [18]	T2W, ADC and DCE MRI	Support vectors machine (method from Vos et al. [13])	Transition zone	Yes
Hambrock et al. [19]	T2W, ADC and DCE MRI	Support vectors machine (method from Vos et al. [13])	Peripheral zone and transition zone	Yes
Unsupervised				
Tiwari et al. [20]	Spectroscopy	Hierarchical	Prostate	No
Liu et al. [21]	T2W, ADC and DCE MRI	Markov random fields	Peripheral zone	Yes
Comparison				
Ozer et al. [22]	T2W, ADC and DCE MRI	Supervised methods support vectors machine and relevance vector machine with unsupervised method; Markov random fields (method from Liu et al. [21])	Peripheral zone	Yes

The methods are grouped into two categories: supervised and unsupervised. Classification is also performed according to the criteria for the MR image sequences used: T2-weighted (T2W), dynamic contrast enhanced (DCE), apparent diffusion coefficient (ADC) computed from the diffusion-weighted (DW) sequences and spectroscopy images, as well as the proton density sequence. The clustering technique used, region of interest (entire gland or specific area, such as the peripheral zone) and the validation with the ground truth from the histopathological maps are also indicated

Methods

Figure 2 depicts the pipeline of the method.

Data preparation: spatial registration and feature extraction

The multiparametric MR sequences could not be processed directly for two reasons. First, most of the images were acquired from different fields of view and thus had different spatial resolutions. Second, there were patient movements between acquisitions. Therefore, the first step was spatial registration and normalization. Because T2W images are regarded as the cornerstone for prostate morphology evaluation, these images were considered the reference space, and the other sequences were strictly registered to this space using standard affine registration algorithms based on maximization of mutual information.

Only a simplest affine registration was considered due to the fact that all the images are acquired during the same MR exam, and thus, we can consider that morphological changes due to rectum and bladder pressures are negligible and therefore no need to the application of a more sophisticated method to compensate the deformations.

Following this spatial matching, resampling and interpolation were used to match the other sequences with the T2W images in terms of resolution.

After this preprocessing, each prostate voxel was described by a feature vector containing the image features as grey levels from the T2W images, the ADC and the pharmacokinetic parameters (K_{trans}, K_{ep} and V_e).

A previous study [23] demonstrated that the local parameters, computed using fractal geometry, allowed for better detection of heterogeneities in prostate tissues from T2W MR images than from the native grey level values. Fractal geom-

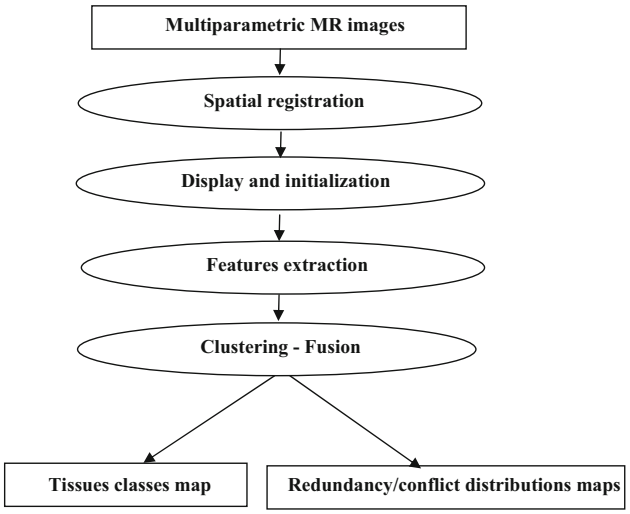

Fig. 2 The pipeline of the method. The multiparametric data are first spatially registered. After feature extraction, evidential theory-based clustering is used to reduce the data into homogeneous classes

etry is a powerful tool for texture analysis that can be used to process medical imaging data efficiently. The fractal geometry can be measured using the fractal dimensions (FDs). We computed the local 3D FDs for each $7 \times 7 \times 3$ region of interest (ROI) using the variance method [24]. Thus, instead of considering the T2W image grey levels, a local fractal dimension was estimated for each voxel.

By combing all of the MR data, a feature set including the local fractal dimension, the ADC value and the pharmacokinetic parameters K_{trans}, V_{e} was associated to each voxel as follows:

$$\text{Voxel}(V_i) = \{\text{FD}, \text{ADC}, K_{\text{trans}}, V_{\text{e}}\} \quad (1)$$

After processing, the data were normalized and standardized for the range of different features. For each feature, the mean and the standard deviation were computed. For each feature value, the mean was then subtracted, and the result was divided by the standard deviation.

Source modelling and clustering

Initialization

Our method was designed to assist radiologists in analysing large numbers of images by fusing the sources into a single map. The voxels were described by their features (Eq. 1) and were grouped into homogeneous patterns. Class initialization is a key step in any clustering process for addressing this issue. Our proposed approach was inspired by radiologists' behaviour when cognitively analysing MR images. Generally, the most sensitive images, typically pharmacokinetic and ADC images, are analysed first to detect and highlight the suspicious regions. To refine the analysis, several cross-analyses are performed using all of the image sequences.

In this regard, the K_{trans} map could be used to define the initial classes map. First, the image histogram was constructed, and a mode recognition algorithm [25] was applied to detect the class number. Then, the K-means algorithm was used for clustering. The results were applied to the remaining image sources to obtain the configuration of the first classes.

Evidential modelling

Evidential reasoning associates a data source or sensor, S, with a set of propositions, also known as the "frame of discernment". In a classification context, the frame of discernment, denoted as Ω, is the set of classes. If $\omega_1, \ldots, \omega_k$ denote these classes, then $\Omega = \{\omega_1, \ldots, \omega_k\}$.

Let $P = \{P_1, \ldots, P_N\}$ be the set of patterns/objects to be assigned to one of the Ω classes. Evidential reasoning allows for the extraction of the partial knowledge of this assignment, called the "basic belief assignment" (bba). A bba is a function that takes values in the range [0, 1] and defines the 2^{Ω} subsets of Ω ($\{\emptyset, \omega_1, \ldots, \omega_k, \omega_1 \cup \omega_2, \ldots,\}$). For each pattern $P_i \in P$, a bba (denoted as m_i) allows us to measure the assignment to each subset A of Ω such that the following relationship is true:

$$\sum_{A \subseteq \Omega} m_i(A) = 1 \quad (2)$$

The higher the value of $m_i(A)$ is, the stronger the belief for assigning P_i to A. For instance, $m_i\left(\{\omega_j\}\right) = 1$ implies that $\left(\forall A \subseteq \Omega, A \neq \{\omega_j\}\right), m_i(A) = 0$. This means that P_i is assigned to $\{\omega_j\}$. However, if $m_i\left(\{\omega_j\}\right) = 0.5$, $m_i(\{\omega_l\}) = 0.2$ and $m_i\left(\{\omega_j, \omega_l\}\right) = 0.3$, there is a stronger belief for assigning P_i to $\{\omega_j\}$ than to $\{\omega_l\}$. It also highlights that there is a 20 % belief for assigning P_i to the union of the 2 classes, which can be interpreted as a doubt regarding pattern membership. In contrast to the fuzzy set model, evidential reasoning can extend the partial membership concept by assigning beliefs not only to classes but also to unions of classes. This feature is particularly useful in cases in which the classes overlap.

Using this model, Denoeux and Masson [26] introduced a new type of data partition called the "credal partition". This partition can be seen as an extension of the fuzzy partition, with bba functions replacing the fuzzy membership functions. The authors later proposed an evidential version of the C-means classifier (the ECM) that used a credal partition, which was inspired by the fuzzy C-means (FCM) algorithm [7]. This algorithm classifies N patterns into k classes of Ω, based on the class centres and the minimization of a cost function. As is the case for fuzzy partitions in FCM, the credal

partition (in which each line is a bbam_i associated with a pattern P_i) is optimized iteratively. Further details on this generic classification method can be found in [7].

Spatial relaxation

The ECM model, as previously described, extracts and optimizes partial knowledge for pattern assignments. The ECM model can be used to classify voxels directly as independent data objects. However, the voxel neighbourhoods, defined by the connexity system, provide valuable information. In fact, the image segmentation supposes that the image regions share common features. Connexity and neighbourhood systems model this assumption using region-oriented segmentation methods, such as growing regions or hidden Markov field models.

In a homogeneous region or class, a bba not only provides information on a pattern but also on its connected neighbours. Corrupted information, extracted from outliers/noise patterns, can be relaxed using the information from neighbours. Thus, introducing neighbourhood information in ECM modelling can provide the following advantages:

- Modelling of contextual region information by extracting information from the patterns/voxels;
- Reduced corrupted information related to outliers and noise; and
- Assimilation of the ECM classifiers into region-based segmentation processes.

The $bbam_i$ of pattern P_i (associated with voxel V_i) was relaxed by combining it with bba functions from spatially connected neighbours. Spatial connection was defined by a 3D connexity system (26 in this study). A combination was performed using a conjunctive bba combination operator [27].

Let m_i be the bba of the pattern P_i and $\{m_{i1}, \cdots, m_{i26}\}$ be the bba functions from P_i's 26 connected neighbours $\{P_{i1}, \cdots, P_{i26}\}$. We denote as m'_i, the result of combining m_i and $\{m_{i1}, \cdots, m_{i26}\}$

$$\begin{array}{l}\forall A \subseteq \Omega \\ m'_i(A) = \sum\limits_{\substack{A_1 \cap \cdots \cap A_f = A \\ A_1 \cdots A_f \subseteq \Omega}} m_i(A_1) \cdots m_{i26}(A_f)\end{array} \tag{3}$$

However, the contribution of each neighbour to this combination should be weighted by its distance from the considered voxel. This combination is particularly relevant for prostate MRI, in which the voxels are significantly anisotropic. Based on this reasoning, the neighbouring bba functions were weighted as follows.

Let m_{ij}^{j} be the result of weighting m_{ij}

$$\begin{array}{l}\forall A \subseteq \Omega \\ \begin{cases} m_{ij}^{\alpha_j}(A) = \alpha_j . m_{ij}(A) \\ m_{ij}^{\alpha_j}(\Omega) = 1 - \alpha_j + \alpha_j . m_{ij}(\Omega) \end{cases}\end{array} \tag{4}$$

where

$$\alpha_{\mathrm{j}} = \frac{\gamma}{\mathrm{d}_{\mathrm{ij}}^2} \tag{5}$$

$0 \leq \gamma \leq 1$ is a parameter, and d_{ij} is a normalized Euclidean distance between voxel v_i and its spatial neighbour v_{ij} . Using Eq. (3) and replacing the neighbouring bba functions with the weighted ones (4), we define m'_i as follows.

$$\begin{array}{l}\forall A \subseteq \Omega \\ m'_i(A) = \sum\limits_{\substack{A_1 \cap \cdots \cap A_f = A \\ A_1 \cdots A_f \subseteq \Omega}} m_i(A_1) \cdot m_{i1}^{\alpha_1}(A_2) \cdots m_{i26}^{\alpha_{26}}(A_f)\end{array} \tag{6}$$

This combination is used as a relaxation step that allows for correction of the evidential assignment of a voxel based on the information from its neighbours.

Decision making

At the level of bba function extraction and optimization, we measure belief for the membership of each voxel to one of the classes $\omega \in$. However, we also measure belief for the empty set and subsets A, which could be interpreted as "doubt" regarding the membership of the voxel. A decision still must be made to classify the voxels into one of the classes. This decision is reached by transforming the bbam_i into a probability measurement, as calculated by

$$\begin{array}{l}\forall \omega_i \in \Omega \\ \mathrm{Prob}(\omega_i) = \frac{1}{1 - m_i(\phi)} \sum\limits_{\substack{\omega \in A \\ A \subseteq \Omega}} \frac{m_i(A)}{|A|}\end{array} \tag{7}$$

where $|A|$ denotes the number of elements in A and ϕ is the emptyset.

Finally, we define the decision rule R that associates the pattern P_i with one of the classes of as follows.

$$R(P_i) = \underset{\omega \in \Omega}{\mathrm{argmax}} \left(\mathrm{Prob}(\omega_i)\right) \tag{8}$$

Results presentation

For the presentation of the results, two levels are proposed. The first level displays a single 3D class map with a colour associated with each class. This map labels all of the voxels with one of the $(\{\omega_1, \ldots, \omega_k\})$ classes. It also renders

the tissue distribution homogeneous. For interpretation purposes, the map can be merged with any of the original image sources.

The second display level provides a more detailed description of the clustering results. The different probability maps resulting from the belief membership conversion (Eq. 7) are displayed using colour maps. These maps could be very useful in addressing conflict regions. Indeed, they include the empty set probabilistic distribution. The empty set is associated with the reject class, grouping all of the voxels that could not be clearly associated with one of the classes (i.e. the probability of the empty set was the greatest).

The maps also include all of the other subset cases.

For instance, for a typical case with 2 classes, $\omega_1 =$ healthy tissue and $\omega_2 =$ suspicious tissue, the clustering produced 4 maps: a probability map for each class and a probability map for the 2 class unions in which a voxel has the same probability of being in either class. The last map is the empty set map, which groups the outliers.

The first level display creates the homogeneous tissue map by combining the 2 results of classes ω_1 and ω_2.

Experiments and results

In this section, we report the results of the method applied to synthetic data with a known ground truth for class distribution and clinical images correlated with histopathology findings.

Simulated image experiments

The aims of these experiments were to test and evaluate the clustering process with regard to noise.

Creation

Simulation of multiparametric MR images is a difficult process. Moreover, a complete simulation should model and simulate the tumour behaviour for all of the MR sequences (T2W, DCE, DWI and spectroscopy). To our knowledge, these behaviours are not yet well known.

Nevertheless, to highlight the performance of the ECM clustering combined with spatial neighbouring relaxation on multisource data, we rendered multiparametric images using 3 MR clinical sequences: T2W, DCE and DWI. For each sequence, a radiologist delineated the peripheral and transition zones. The transition zone (TZ) was then filled with its mean value. The peripheral zone (PZ) level was deduced using a predetermined contrast value C defined as

$$C = \frac{|I_{TZ} - I_{PZ}|}{|I_{TZ} + I_{PZ}|} \tag{9}$$

where I_{TZ} and I_{PZ} are the mean MR signals of TZ and PZ in the considered sequence, respectively.

Gaussian noise was added, and a median filter was applied to reduce the salt-pepper aspect of the noisy images so that they would be more similar to the real data. Figure 3 illustrates this process.

The signal-to-noise ratio of the simulated data was defined as:

$$\mathrm{SNR_{db}} = 10\log\left[\frac{\sum_{i=1,\ldots,\mathrm{n}} (I_0)^2}{\sum_{i=1,\ldots,n} (I - I_0)^2}\right] \tag{10}$$

where I_0 and I are the intensities before and after adding the Gaussian noise, respectively.

Finally, the rendered images had different quality levels. The signal-to-noise ratios ranged from 18.21 to 7.77 dB, and the contrast levels (C, Eq. 9) ranged from 0.1 to 0.25.

Results

The evaluation of the classification method for the synthetic data consisted of the accurate segmentation of the peripheral and transition zones. The evaluation was performed using the classification error from the voxel labelling.

Figure 4 illustrates the classification errors observed for different noise levels.

Real data evaluation

Description

For clinical evaluation, we considered the abilities of the method to segment cancerous regions. For this purpose, a retrospective study was done. Multiparametric MR images were collected from 15 patients using a Philips ACHIVA 1.5T machine. The data consisted of T2W images with a $0.48 \times 0.48 \times 4.00\ \mathrm{mm}^3$ voxel size (15 slices by volume), T1W DCE MRI images with a $0.61 \times 0.61 \times 4.00\ \mathrm{mm}^3$ voxel size (15 slices by volume, 20 dynamics) and an ADC map computed from 2 DWI acquisitions using b=0 and b=600 with a $1.12 \times 1.12 \times 4.00\ \mathrm{mm}^3$ voxel size (15 slices by volume). The DCE images were processed in-house using software implementing Tofts' model to generate the pharmacokinetic K_{trans}, V_{e} and K_{ep} maps.

As described above, the MR volumes were registered and interpolated to fit the T2W resolution.

All of the patients underwent radical prostatectomy. To have a true diagnosis, the histological findings were correlated with MRI data. The prostate specimens were stained, fixed and sectioned according to the Stanford protocol [28]. A

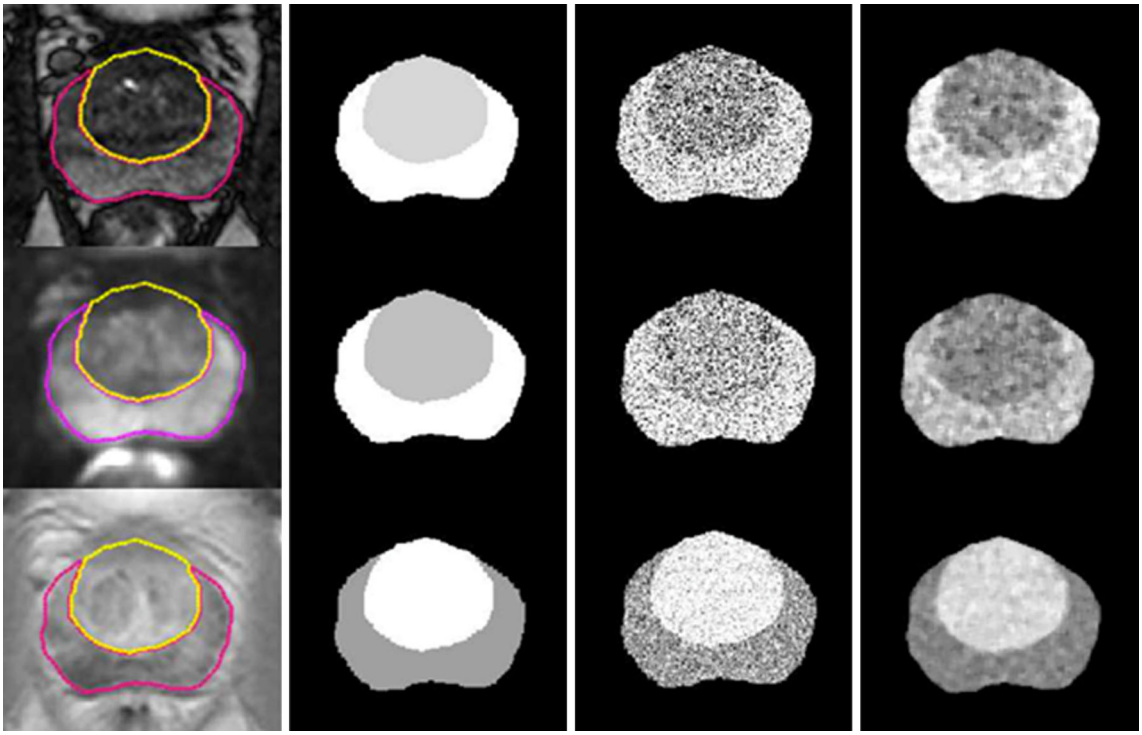

Fig. 3 The image simulation process. From *left* to *right*, original MRI with predelineated peripheral and transition zones, the zones labelled with their respective mean level, data with Gaussian noise and data after a smoothing median filter. The *first*, *second* and *third lines* represent the T2W, DWI and DCE images, respectively

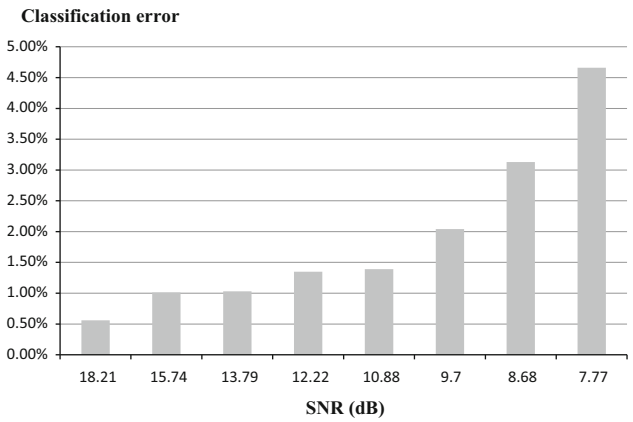

Fig. 4 The results expressed as classification errors for labelling voxels belonging to either the peripheral or transition zones from multisource data with different noise levels

reconstructed histological map of each prostate was created. The contours of the histological zones, as well as the outlines of each cancer, were drawn on the slides under a microscope (Fig. 5a). The results from these analyses were reported on the MR images by manual correspondence with the histology images (Fig. 5b). This task was performed by experienced uro-radiologists, according to the method described in [29]. The prostate was divided into eight regions of interest by the octant technique. The top and bottom were divided into four quadrants, corresponding to the transition zone (TZ) and peripheral zone (PZ) on the left and right. Within each octant, the TZ, PZ and anterior fibromuscular stromal boundaries were traced. The tumour was located according to these histological zone boundaries.

Out of 15 patients, a total of 43 tumours were considered, including 25 tumours with a volume greater than 0.5 cc (Table 2).

Results

For quantitative evaluation, we measured the ability of the method to distinguish tumour patterns from healthy tissue patterns. For this purpose, at the end of the clustering process, the resulting 3D map was merged with the anatomical T2W MR images, allowing to the radiologist to label and associate the different classes to the tissue classes (peripheral zone, transition zone, etc.) and thus isolate the suspicious regions (tumours). By comparing the results to the actual diagnosis for each patient, the numbers of true positives, false positives, true negatives and false negatives were evaluated for different regions of interest. Sensitivity and specificity were computed, respectively, as follows:

$$\text{sensitivity} = \frac{\text{true positives}}{\text{true positives} + \text{false negatives}}$$

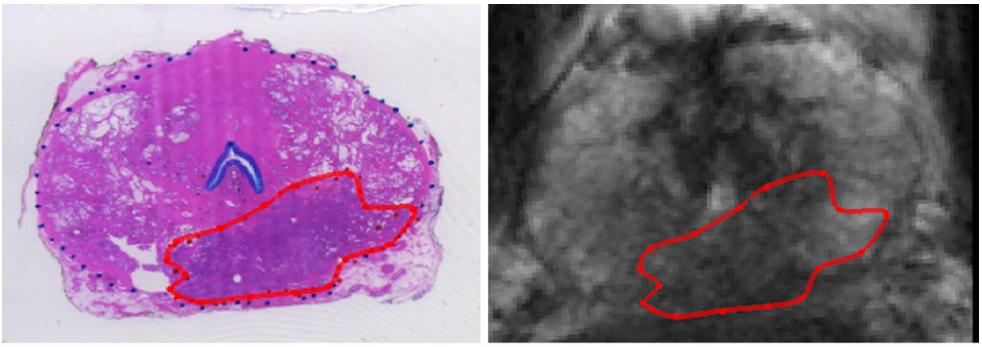

(a) **(b)**

Fig. 5 **a** Histopathology image. **b** Cancer maps created from the histopathology images

Table 2 Histopathologic analysis of the 15 patients included in the study

Patients	Number of cancers	Number of cancers with volume >0.5 cc
1	3	2
2	3	1
3	2	1
4	4	2
5	3	1
6	2	2
7	4	3
8	3	1
9	4	3
10	2	2
11	2	1
12	5	3
13	1	0
14	1	1
15	4	2

$$\text{specificity} = \frac{\text{true negatives}}{\text{true negatives} + \text{false positives}}$$

The Dice (DSC) measure was also calculated as:

$$\text{DSC} = \frac{2.|S \cap G|}{|S| + |G|}$$

where S and G are the segmentation and the ground-truth results, respectively, while $|.|$ operator denotes the pixels number in the set.

Table 3 summarizes the obtained results. The mean sensitivity and specificity were 65 % (0–100 %) and 81% (50–100 %), respectively. The worst scores corresponded to tumours with volumes less than 0.5 cc. This value is currently accepted as a limit for tumour detection on MR imaging. By considering only tumours with volumes greater than the 0.5 cc threshold, the mean sensitivity and specificity grew to 70 and 88 %, respectively.

Table 3 Quantitative evaluation of the proposed method

	Sensitivity	Specificity	Dice
All cancers	65 % (0–100 %)	81 % (50–100 %)	0.56 ± 0.12
Cancers >0.5 cc	70 % (68–100%)	88 % (82–100 %)	0.65 ± 0.07

Figure 6 shows a case in which 3 classes were detected. The result (Fig. 6f) depicts the class map, which highlights a class for the peripheral zone, a class for the transition zone tissue and a third class composed of data from 2 patterns that could be interpreted as a tumour. Returning to the MR images, one of these patterns was clearly depicted in the 4 images (T2W, ADC, K_{trans} and V_{e}), while the second was only visible as a hyper-vascular area on the K_{trans} map. The fusion allowed us to place these two patterns in the same class. The ground truth image (G) revealed two tumours (circles).

Figure 7 depicts a case in which the analysis focused only on the peripheral zone, using 3 sources: the T2W (Fig. 7a), the K_{trans} (Fig. 7b) and the ADC (Fig. 7c) maps. Initialization was performed starting with the ADC map. The result of the fusion (Fig. 7e) is displayed in the superposition mode for the T2W image, whereas Fig. 7d shows the bba map. Both maps (d and e) highlight a region corresponding to the optimal fusion among the hypo-signal of the ADC map, the hyper-signal of the K_{trans} and the T2W hypo-signal. Figure 7f shows the ground truth.

As a last experiments and in order to highlight to proposed method efficiency, the obtained results were compared to one of the literature approaches. As it was indicated in the "Introduction" section and in Table 1, two methods classes exist: supervised algorithms needing a learning step and unsupervised algorithms without a learning step. Since our aim was to investigate a clustering technique to perform an unsupervised analysis of the image, the closest method from Table 1 to the

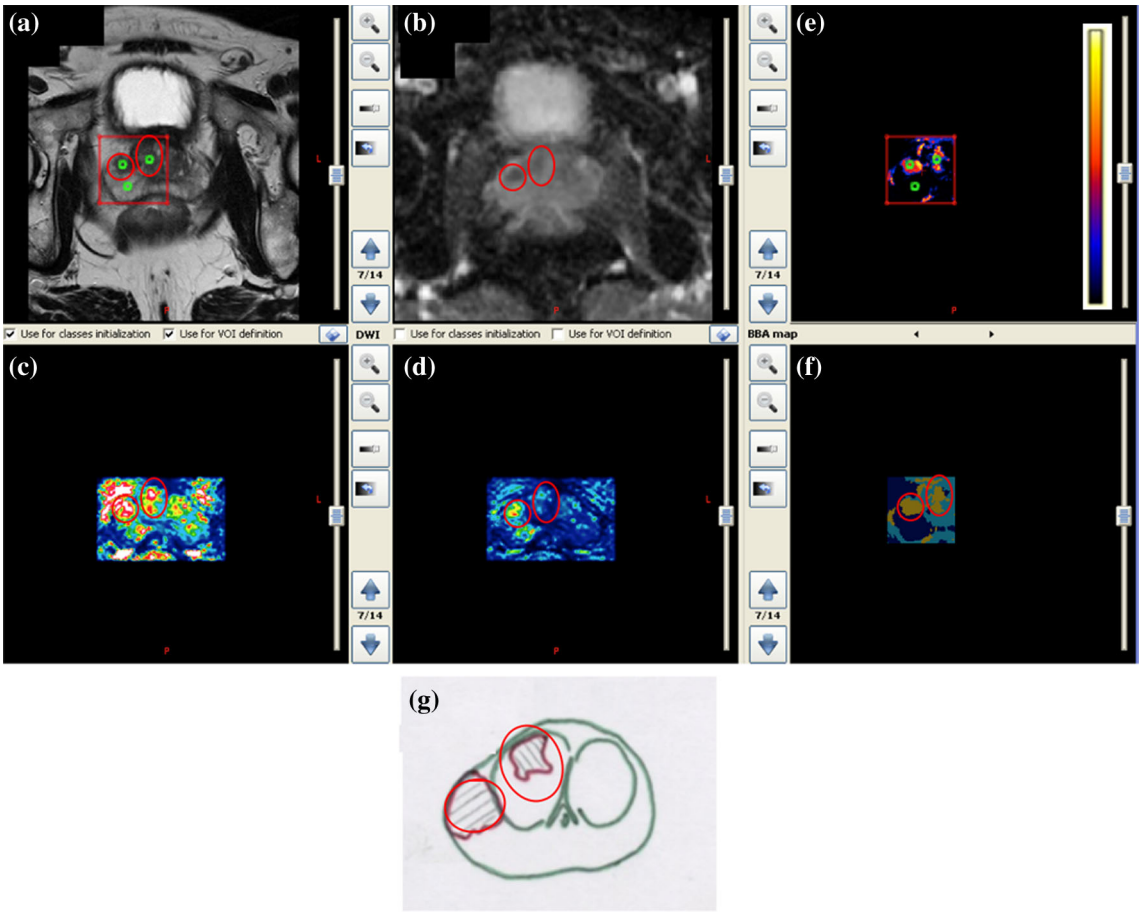

Fig. 6 Classification results—Example 1. **a** T2W image with the region of interest to be analysed. Three tissues are defined: part of the PZ, part of the TZ and a suspected area. **b** The ADC map. **c** The K_{trans} map. **d** The V_{e} map. **e** Basic belief assignment (bba) map showing the membership degree of each voxel to the 3 classes. **f** Fusion map showing the distribution of the 3 tissues. *Each colour* is associated with a class. **g** The ground truth

proposed method is the one by Liu et al. [21]. This method is unsupervised and acts on MP MRI. The fuzzy random field modelling was implemented as described (Table 4).

Discussion: Conclusion

In this study, we described an unsupervised fusion scheme to analyse multiparametric MR images. This proposed framework was not designed for cancer detection or characterization but rather as a tool to assist radiologists in analysing multisource data. Because it is fully automatic, it can be applied in clinical routines for preliminary analysis and to fuse multiple MR sequences into a single 3D map in which the voxels that exhibit similar behaviours in all of the sequences are grouped into classes.

The method is based on a spatial registration and a normalization step that standardizes the data, followed by a multisource clustering step that is driven by the evidential C-means algorithm. A relaxation step is introduced in this algorithm to integrate the voxel spatial neighbourhood information. As a result of this relaxation, the basic belief for the assignment of each voxel can be corrected using information from connected neighbours, via a conjunctive combination of the bba functions.

The combination of the ECM algorithm with this spatial relaxation allowed us to perform clustering and segmentation on simulated multisource data with different noise levels (Fig. 3), with accuracy of 95 % (Fig. 4).

Two-level result reporting was proposed. The first level used a single map that represented homogeneous tissue distribution, while the second level was a membership degrees image. This image maps the source conflict regions.

We validated our method by analysing clinical data from 15 patients. The method had mean sensitivity and specificity of 65 and 81 %, respectively. These tests considered data consisting of grouped tumours, with different volumes from both the peripheral zone and the transition zone.

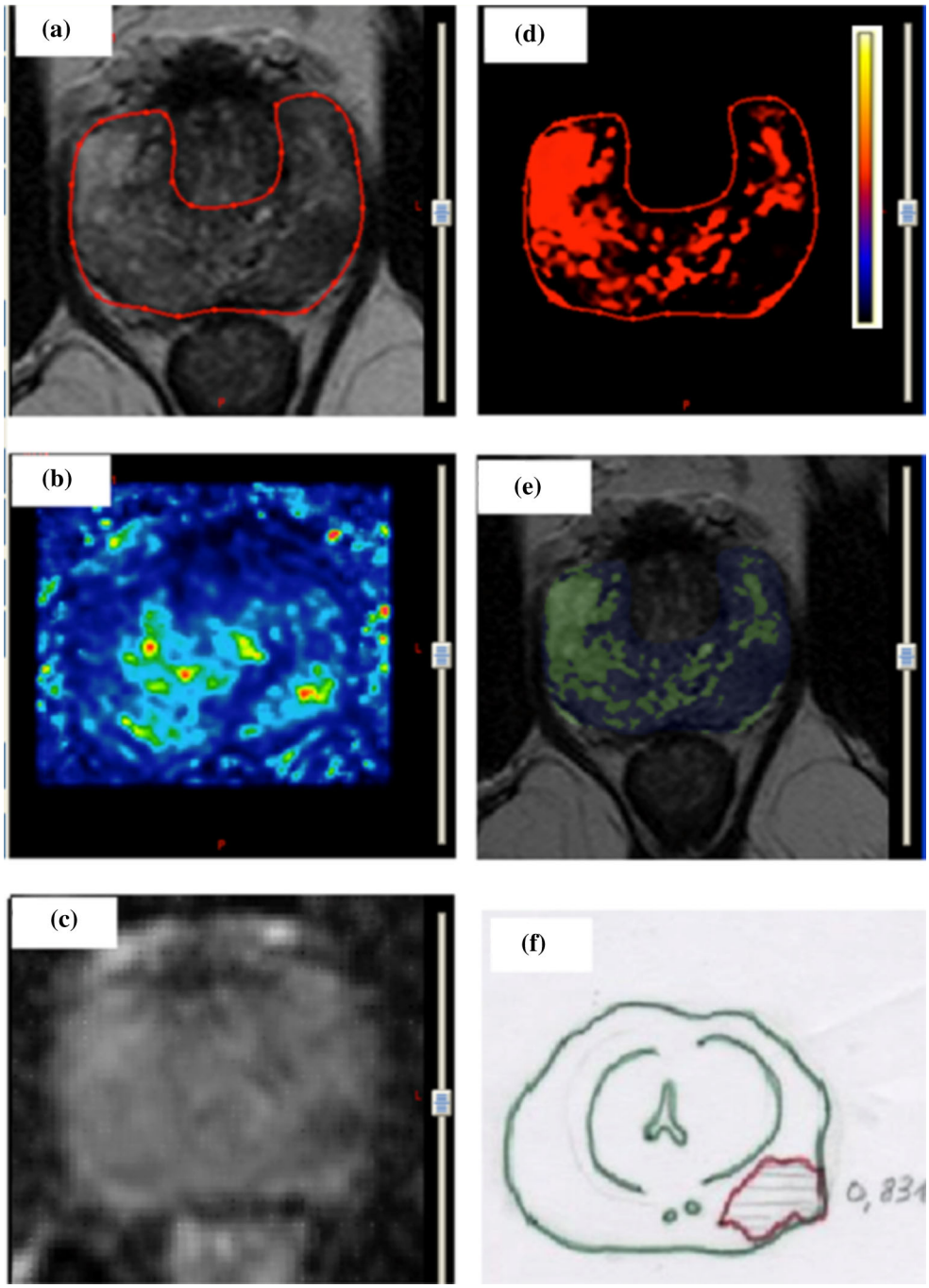

Fig. 7 Classification results—Example 2. **a** T2W image with peripheral zone delineation. **b** The K_{trans} map. **c** The ADC map. **d** The basic belief map. **f** The fusion map of images (**a**), (**b**) and (**c**). Each colour is associated with a class. The result is merged with the T2W (**a**) image. **f** The ground truth

To our knowledge, there has been only one previously published study, by Liu et al. [21], in which the authors used an unsupervised classification method to diagnose prostate cancer using multiparametric MR images. The method was based on fuzzy Markov random fields, in which the parameters were implicitly estimated and combined with the segmentation process. However, the previous method was parametric because Gaussian distributions were assumed for the classes. Our approach was free from any assumptions regarding class distributions.

Compared with the previously reported methods, which have mainly been based on supervised classification algorithms, our results might appear weak. Indeed, the supervised techniques described in Table 1 reported sensitivity and

Table 4 Comparison of the proposed method with the Lui et al. method

	Sensitivity	Specificity	Dice
Proposed method	65 % (0–100 %)	81 % (50–100 %)	0.56 ± 0.12
Liu et al. method	63 % (0–100 %)	78 % (52–100 %)	0.50 ± 0.14

Experiments were realized by considering the complete cancer base

specificity scores of at least 85 %. However, as discussed in the "Introduction" section, supervised classification requires an extensive learning process, and the most important issue with this type of approach is that the learning step must be updated each time the data change due to changes in the acquisition protocol.

In a study by Ozer et al. [22], two supervised methods were compared with an unsupervised algorithm (Liu et al. [21]). It was concluded that the supervised algorithms performed better than the unsupervised algorithm. In general, when the data are similar to those used during the learning process, in which all of the classification parameters are optimized, supervised approaches outperform unsupervised approaches. This situation changes if new data are used. In clinical practice, such a change often occurs due to changes in the acquisition protocols, when new MR sequences parameters or new machine are used.

Without the inclusion of any learning or calibration steps, the preliminary results for our unsupervised approach to computer-aided analysis of multiparametric MR images showed promising results. Moreover, the global framework described here could be extended to other multimodality sources. Indeed, photon emission tomography (PET) has the ability to analyse quantitative biomarkers that assess a host of physiological and biochemical tumour characteristics. Ultrasound elastography could also be valuable for tissue characterization. The only limitation for the integration of all of these sources into the proposed approach is spatial registration.

The fusion strategy employed in this study attributed equally distributed confidence levels to the different image sources. However, specific parameterization using different weights is also possible. Tiwari et al. [30] investigated the weighted combination of multiparametric MR imaging for the evaluation of radiation therapy outcomes, and they reported promising results. The weighted combination of multiparametric or multimodality sources provided specific confidence levels for each imaging modality, according to its sensitivity and specificity. This combination could easily be applied for basic belief assignment modelling. It could also be used at different stages during initialization or before final fusion and conversion of the bba functions into class membership degrees.

Another important issue concerns validation. The evaluation described here was a single-observer study. Currently, we are preparing a more extensive evaluation with a more relevant patient base and better selection criteria, such as limitation to only one zone (peripheral or transition zones) and consideration of only clinically significant tumours larger than the threshold of 0.5 cc. This evaluation will be a multi-observer study.

Lastly, it is understood that the proposed approach will not replace supervised approaches. As clearly indicated, our method is not a diagnostic technique. The development and implementation of supervised techniques for distinguishing aggressive tumours from benign lesions remain of great importance to clinical practice.

Conflict of interest Nacim Betrouni, Nasr Makni, Said Lakroum, Philippe Puech, Arnauld Villers and Serge Mordon declare that they have no conflict of interest.

Informed consent Informed consent was obtained from all patients for being included in the study.

References

1. Tanimoto A, Nakashima J, Kohno H, Shinmoto H, Kuribayashi S (2007) Prostate cancer screening: the clinical value of diffusion-weighted imaging and dynamic MR imaging in combination with T2-weighted imaging. J Magn Reson Imaging 25(1):146–152
2. Tofts PS, Berkowitz B, Schnall MD (1995) Quantitative analysis of dynamic Gd-DTPA enhancement in breast tumors using a permeability model. Magn Reson Med 33(4):564–568
3. Quantitative Imaging Biomarkers Alliance (2012) DCE MRI Quantification profile. http://rsna.org/QIBA_.aspx
4. Bloch I (1996) Some aspects of dempster-shafer evidence theory for classification of multi-modality medical images taking partial volume effect into account. Pattern Recogn Lett 17(8):905–920
5. Capelle AS, Colot O, Fernandez-Maloigne C (2004) Evidential segmentation scheme of multi-echo MR images for the detection of brain tumors using neighborhood information. Inf Fusion 5(3):203–216
6. Chen SYJ, Lin WC, Chen CT (1993) Evidential reasoning based on Dempster-Shafer theory and its application to medical image analysis. Neural Stoch Methods Image Signal Process II 2032:35–46
7. Masson MH, Denoeux T (2011) ECM:An evidential version of the fuzzy c-means algorithm. Pattern Recogn 41:1384–1397
8. Makni N, Iancu A, Colot O, Puech P, Mordon S, Betrouni N (2011) Zonal segmentation of prostate using multispectral magnetic resonance images. Med Phys 38(11):6093–6105
9. Chan W, Wells R, Mulkern S, Haker J, Zhang K, Zou S, Maier, Tempany C (2003) Detection of prostate cancer by integration of line-scan diffusion, t2-mapping and t2-weighted magnetic resonance imaging: a multichannel statistical classifier. Med Phys 30(9):2390–2398
10. Madabhushi A, Feldman MD, Metaxas DN, Tomaszeweski J, Chute D (2005) Automated detection of prostatic adenocarcinoma from high-resolution ex vivo MRI. IEEE Trans Med Imaging 24(12):1611–1625
11. Vos PC, Hambrock T, Hulsbergen-van de Kaa CA, Fütterer JJ, Barentsz JO, Huisman HJ (2008) Computerized analysis of prostate lesions in the peripheral zone using dynamic contrast enhanced MRI. Med Phys 35(3):888–899

12. Puech P, Betrouni N, Makni N, Dewalle AS, Villers A, Lemaitre L (2009) Computer-assisted diagnosis of prostate cancer using DCE-MRI data: design, implementation and preliminary results. Int J Comput Assist Radiol Surg 4:1–10
13. Vos PC, Hambrock T, Barenstz JO, Huisman HJ (2010) Computer-assisted analysis of peripheral zone prostate lesions using t2-weighted and dynamic contrast enhanced t1-weighted MRI. Phys Med Biol 55(6):1719
14. Lopes R, Ayache A, Makni N, Puech P, Villers A, Mordon S, Betrouni N (2011) Prostate cancer characterization on MR images using fractal features. Med Phys 38(1):83–95
15. Niaf E, Rouvière O, Mège-Lechevallier F, Bratan F, Lartizien C (2012) Computer-aided diagnosis of prostate cancer in the peripheral zone using multiparametric MRI. Phys Med Biol 57(12):3833–3851
16. Shah V, Turkbey B, Mani H, Pang Y, Pohida T, Merino M, Pinto PA, Choyke PL, Bernardo M (2012) Decision support system for localizing prostate cancer based on multiparametric magnetic resonance imaging. Med Phys 39(7):4093–4103
17. Chesnais AL, Niaf E, Bratan F, Mège-Lechevallier F, Roche S, Rabilloud M, Colombel M, Rouvière O (2013) Differentiation of transitional zone prostate cancer from benign hyperplasia nodules: evaluation of discriminant criteria at multiparametric MRI. Clin Radiol 68(6):323–330
18. Hoeks CMA, Hambrock T, Yakar D, Hulsbergen-van de kaa CA, Feuth T, Witjes JA, Fütterer JJ, Barentsz JO (2013) Transition zone prostate cancer: detection and localization with 3-T multiparametric MR imaging. Radiology 266:207–217
19. Hambrock T, Vos PC, Hulbergen-van de Kaa CA, Barentsz JO, Huisman HJ (2013) Prostate cancer: computer-aided diagnosis with multiparametric 3-T MR imaging-effect on observer performance. Radiology 266(521):530
20. Tiwari P, Rosen M, Madabhushi A (2009) A hierarchical spectral clustering and nonlinear dimensionality reduction scheme for detection of prostate cancer from magnetic resonance spectroscopy (MRS). Med Phys 39(9):3927–3939
21. Liu X, Langer DL, Haider MA, Yang Y, Wernick MN, Yetik (2009) Prostate cancer segmentation with simultaneous estimation of markov random field parameters and class. IEEE Trans Med Imaging 28(6):906–915
22. Ozer S, Langer D, Liu X, Haider M, van der Kwast T, Evans A, Yang Y, Wernick M, Yetik I (2010) Supervised and unsupervised methods for prostate cancer segmentation with multispectral MRI. Med Phys 37(4):1873–1883
23. Lopes R, Ayache A, Makni N, Puech P, Villers A, Mordon S, Betrouni N (2011) Prostate Cancer characterization on MR images using fractal features. Med Phys 38(1):83–95
24. Lopes R, Betrouni N (2009) Fractal and multifractal analysis: a review medical image analysis. Med Image Anal 13(4):634–649
25. Postaire JG, Vasseur C (1981) An approximate solution to normal mixture identification with application to unsupervised pattern classification. IEEE Trans Pattern Anal Mach Intell 3(2):163–179
26. Denoeux T, Masson MH (2004) Evidential clustering of proximity data. IEEE Trans Syst Man Cybern 34:95–109
27. Smets P (2007) Analyzing the combination of conflicting belief functions. Inf Fusion 8(4):387–412
28. McNeal JE, Haillot O (2001) Patterns of spread of adenocarcinoma in the prostate as related to cancer volume. Prostate 49:48–57
29. Puech P, Potiron E, Lemaitre L, Leroy X, Haber GP, Crouzet S, Kamoi K, Villers A (2009) Dynamic contrast-enhanced–magnetic resonance imaging evaluation of intraprostatic prostate cancer: correlation with radical prostatectomy specimens. Urology 74(5):1094–1099
30. Tiwari P, Viswanath S, Kurhanewicz J, Madabhushi A (2011) Weighted combination of multi-parametric MR imaging markers for evaluating radiation therapy related changes in the prostate. In: Prostate cancer imaging. Image analysis and image-guided interventions. Lecture notes in computer science, vol 6963. Springer, Berlin, Heidelberg, pp 80–91